ARTICLES
https://doi.org/10.1038/s44160-022-00153-x

nature synthesis

Check for updates

Photoelectrocatalytic biosynthesis fuelled by microplastics

Jinhyun Kim[1], Jinha Jang[1], Thomas Hilberath[2], Frank Hollmann[2] and Chan Beum Park[1]✉

Biocatalytic artificial photosynthesis integrates photocatalysis and redox biocatalysis to synthesize value-added chemicals using solar energy. However, this nature-inspired approach suffers from sluggish rates of reaction because of challenging water oxidation kinetics. Here we report photoelectrochemical biosynthetic reactions that use non-recyclable real-world poly(ethylene terephthalate) (PET) microplastics as an electron feedstock. A Zr-doped haematite photoanode extracts electrons from hydrolysed PET solutions obtained from post-consumer PET waste, such as drinks bottles, and transfers the electrons to the bioelectrocatalytic site. Carbon-based cathodes receive the electrons to activate redox enzymes (for example, unspecific peroxygenase, L-glutamate dehydrogenase and ene-reductase from the old yellow enzyme family) that drive various organic synthetic reactions. These reactions include oxyfunctionalization of C–H bonds, amination of C=O bonds and asymmetric hydrogenation of C=C bonds. These photoelectrocatalytic-biocatalytic hybrid reactions achieve total turnover numbers of 362,000 (unspecific peroxygenase), 144,000 (L-glutamate dehydrogenase) and 1,300 (old yellow enzyme). This work presents a photoelectrocatalytic approach for integrating environmental remediation and biocatalytic photosynthesis towards sustainable solar-to-chemical synthesis.

Plastics have become indispensable in our modern life; worldwide, approximately 390 million tonnes of polymers are produced annually[1]. The recent outbreak of the coronavirus pandemic has further stimulated the global demand for plastics because of the increased use of packaging materials and personal protective equipment[2]. The majority of plastic waste has been incinerated or has accumulated in landfill sites and the natural environment[1], representing a severe loss of valuable resources (for example, an annual loss of 80–120 billion US dollars to the global economy)[3,4]. Furthermore, microplastics—defined as plastics smaller than 5 mm—are imposing serious ecological and environmental threats[1,5]. Microplastics originate via the direct input from a variety of products (for example, cosmetic beads and clothing fibres) or the degradation of plastic debris in the ocean environment. The small size and dilution of microplastics hinders proper collection and reuse, making them ubiquitous in oceans and even drinking water[6].

To address the issue of plastic waste, plastics recycling is desirable but its execution is challenging because of mediocre waste management, deficiencies in recognition of the problem and the complex chemical makeup of plastics[3,4]. For example, approximately 50% of PET is not collected for recycling, although PET is the most copious polyester plastic with an annual production of around 38 million tonnes globally for textiles and packaging[1]. Only 7% of PET bottles are remoulded into bottles, but recycled PET is still hampered by the loss of mechanical properties during the recycling process[7]. Chemical upcycling has been considered as an alternative approach to convert non-recyclable plastic waste into valuable chemicals and materials[3].

Here we report a solar-driven biocatalytic photoelectrochemical (BPEC) platform using non-recyclable real-world PET microplastics as an electron feedstock to synthesize value-added compounds through the combination of photoelectrocatalysis and redox biotransformations, including oxyfunctionalization of C–H bonds, reductive amination of C=O bonds and *trans*-hydrogenation of C=C bonds. As illustrated in Fig. 1, the BPEC system comprises three components. First, a zirconium-doped haematite (Zr:α-Fe_2O_3) photoanode to extract electrons from hydrolysed PET solutions obtained from post-consumer commercial PET waste. Second, a carbon fibre paper (CFP) or anthraquinone-2-carboxylic acid-anchored CFP (AQC/CFP) cathode to generate 1,4-dihydronicotinamide adenine dinucleotide (NADH) or H_2O_2, respectively. Third, a redox enzyme, such as NADH-dependent L-glutamate dehydrogenase (GDH), NADH-dependent ene-reductase from the old yellow enzyme (OYE) family, or H_2O_2-dependent unspecific peroxygenase (UPO), to drive the synthetic reactions. The Zr:α-Fe_2O_3|CFP-based systems exhibit a broad applicability to other enzymatic substrates and show high total turnover numbers (TTNs) for the enzymes of 362,000 (UPO), 144,000 (GDH) and 1,300 (OYE), which surpass those of state-of-the-art BPEC systems using water as an electron feedstock.

Results

Bioelectrocatalytic oxyfunctionalization. We tested a CFP electrode for reductive activation of redox enzymes. The rationale of selecting electrically conductive CFP was its high chemical stability, large surface area and good mechanical strength[8]. The CFP electrode showed randomly oriented microfibres with carbon-based functional groups (for example, conjugated C=C, C–C, C–OH and COOH). In-depth structural characterization via scanning electron microscopy (SEM), X-ray photoelectron spectroscopy and Raman spectroscopy are shown in Supplementary Fig. 1.

For the electrocatalytic production of H_2O_2, we prepared an AQC/CFP electrode using a solution immersion process (for details see Methods). The redox behaviour of AQC on the CFP was confirmed using cyclic voltammetry under reaction conditions representative for peroxygenase reactions[9] (potassium phosphate (KPi) buffer (100 mM, pH 6.0)). The AQC/CFP electrode exhibited a

[1]Department of Materials Science and Engineering, Korea Advanced Institute of Science and Technology (KAIST), Daejeon, Republic of Korea. [2]Department of Biotechnology, Delft University of Technology, Delft, The Netherlands. ✉e-mail: parkcb@kaist.ac.kr

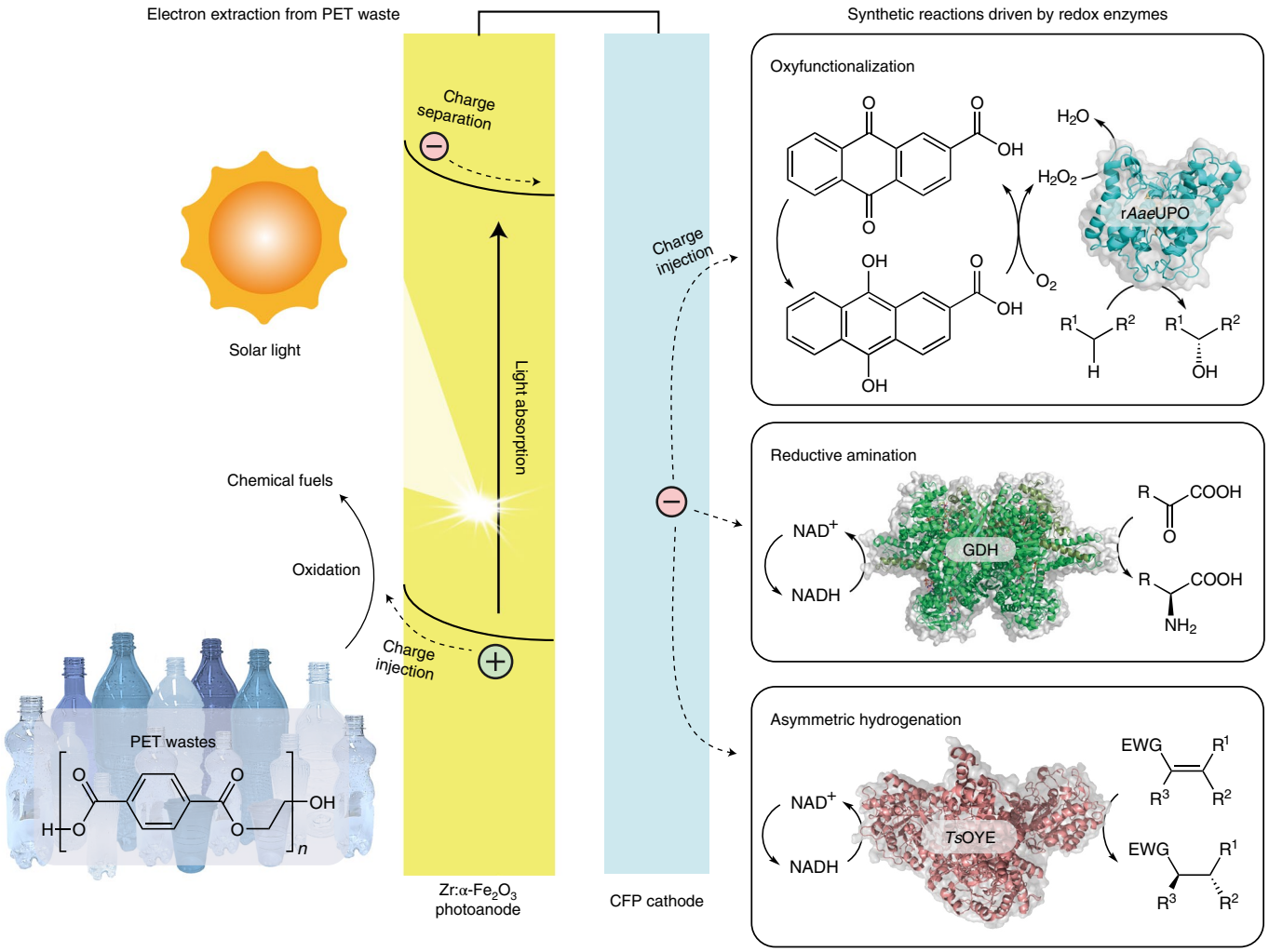

Fig. 1 | Schematic diagram of solar-powered photoelectrochemical biosynthetic reactions using non-recyclable real-world PET microplastics. CFP-based cathodes reduce O_2 to H_2O_2 for biocatalytic oxyfunctionalization and NAD^+ to NADH for enzymatic amination and asymmetric hydrogenation. For the biocatalytic synthesis, a Zr:α-Fe_2O_3 photoanode extracts electrons from hydrolysed PET solutions obtained from post-consumer PET waste. The BPEC systems produce value-added compounds at both electrodes with excellent TTNs of the redox enzymes. NAD^+, nicotinamide adenine dinucleotide; EWG, electron-withdrawing group. Protein structures were rendered using the PyMOL Molecular Graphics System version 2.1.1 (Schrödinger).

redox wave with a formal potential of around 0.1 V versus the reversible hydrogen electrode (RHE) under an argon-enriched environment, whereas the bare CFP did not show the characteristic redox peak (Fig. 2a). We attribute the wave to a typical two-electron–two-proton reduction and oxidation[10] of AQC/$AQCH_2$. The surface concentration of AQC was estimated to be 18 nmol cm^{-2} from its cyclic voltammogram. On purging the electrolyte solution with O_2, a cathodic current of AQC/CFP was much higher than that of CFP (Fig. 2a), indicating an important role of AQC in O_2 reduction.

We confirmed that AQC promotes the reduction of O_2 to H_2O_2. As shown in Fig. 2b, the rate of H_2O_2 production in the AQC/CFP system was 1.85 ± 0.07 mM h^{-1} at 0.16 V_{RHE}. The rate decreased to 0.90 ± 0.04 mM h^{-1} in the absence of AQC. These results highlight AQC-driven facilitation of the interfacial electron-transfer process; our electrochemical impedance spectroscopic analysis shows that the charge-transfer resistance of AQC/CFP is lower than that of CFP under O_2-rich conditions (Supplementary Fig. 2 and Supplementary Table 1). Under anaerobic conditions, H_2O_2 formation was negligible (<0.06 mM h^{-1}; Supplementary Fig. 3). We further confirmed that the AQC/CFP-driven formation of H_2O_2 proceeds via a two-step, single-electron reduction of O_2 (Supplementary Fig. 4).

Having demonstrated in situ H_2O_2 production using the AQC/CFP cathode, we advanced to coupling AQC/CFP-driven electrocatalysis with peroxygenase-catalysed oxyfunctionalization reactions. We selected the recombinant, evolved peroxygenase from *Agrocybe aegerita* (r*Aae*UPO)[11,12], which exhibits a high activity towards the oxidation of C–H bonds. Selective C–H oxyfunctionalization is a dream reaction in synthetic organic chemistry because of the kinetically inert nature of C–H bonds[11,13]. Peroxygenases are promising catalysts for such challenging oxyfunctionalization reactions because they combine a high catalytic activity with high selectivity while depending on simple H_2O_2 as the only oxidant. The application of 0.16 V_{RHE} to the AQC/CFP cathode drove the hydroxylation of ethylbenzene to enantiopure (*R*)-1-phenylethanol (e.e. > 99%) with a formation rate of 1.63 ± 0.08 mM h^{-1}, corresponding to a turnover frequency (TOF) for r*Aae*UPO (that is, $TOF_{rAaeUPO}$) of $32{,}700 \pm 1{,}500$ h^{-1} (Fig. 2c). The bioelectrocatalytic reaction required active r*Aae*UPO, the substrate and an electrical bias (Fig. 2c).

Bioelectrocatalytic amination and hydrogenation. We examined the electrocatalytic capability of CFP to regenerate enzymatically active NADH from NAD^+. $[Cp^*Rh(bpy)H_2O]^{2+}$ (M_{ox}; $Cp^* = C_5Me_5$,

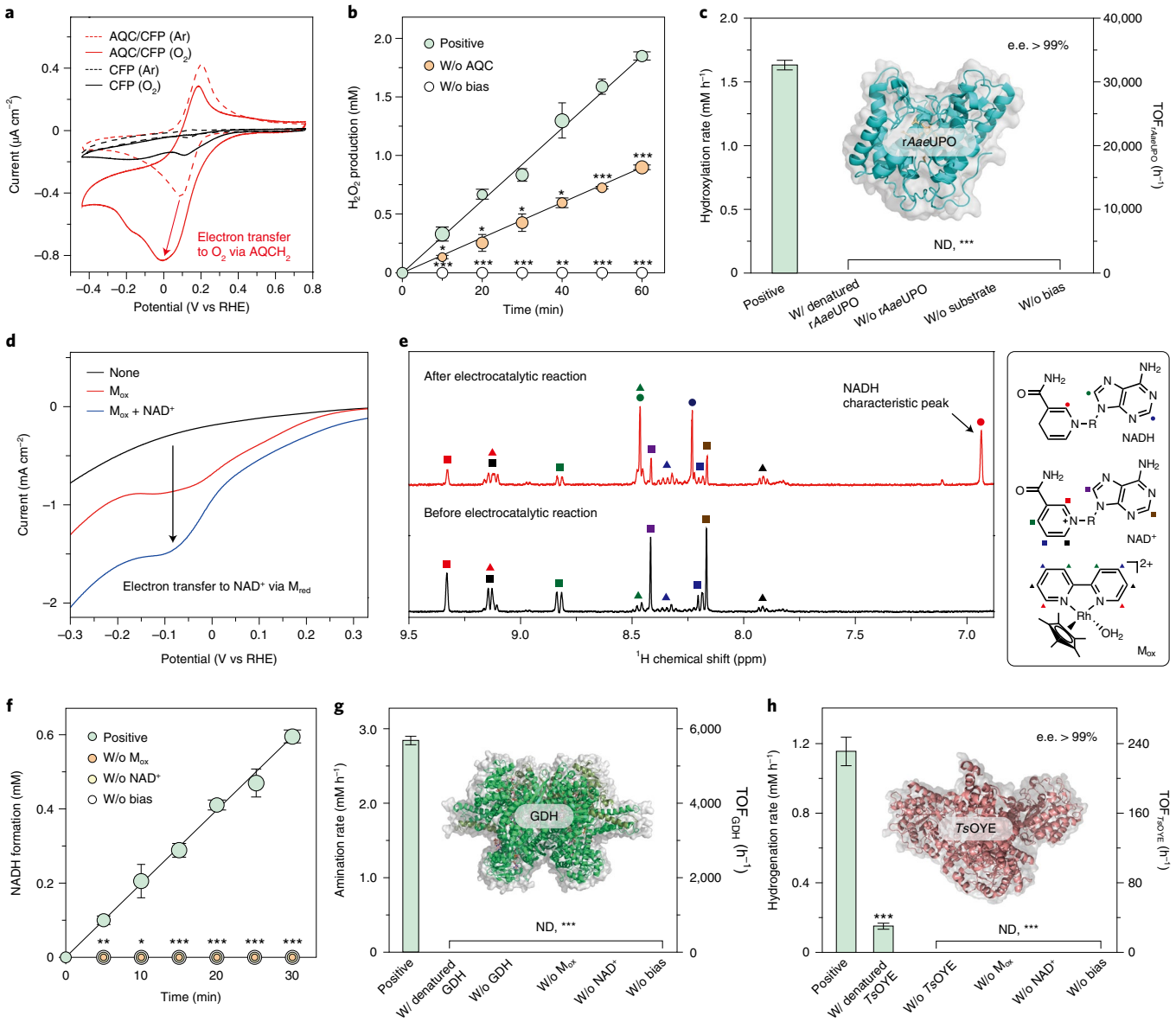

Fig. 2 | Bioelectrocatalytic synthesis using CFP-based materials. a, Cyclic voltammograms of AQC/CFP and CFP cathodes under O_2- or argon-enriched environments. Electrolyte solution, KPi buffer (100 mM, pH 6.0). **b**, Time profiles of electrocatalytic production of H_2O_2. Electrolyte solution, O_2-rich KPi buffer (100 mM, pH 6.0). **c**, Bioelectrocatalytic hydroxylation reaction using AQC/CFP and r*Aae*UPO. **d**, Linear sweep voltammograms for NAD^+ reduction. **e**, ^1H nuclear magnetic resonance spectra before and after the electrocatalytic reaction. The molecular structures of NADH, NAD^+ and M_{ox} are shown in the right panel. Reaction time, 40 min. **f**, Electrochemical production of NADH from NAD^+ using CFP cathode. **g**, Series of control experiments for bioelectrochemical amination using GDH. **h**, Control experiments for enzymatic electrochemical hydrogenation using *Ts*OYE. In **d**–**h**, working electrode is CFP. In **a**–**h**, geometrical surface area of cathode is 1 cm^2 and reaction temperature is 303 K. Applied biases are 0.16 V_{RHE} (**b**,**c**) and −0.2 V_{RHE} (**e**–**h**). In **a**,**d**, scan rate is 25 mV s^{-1}. The error bars correspond to the standard deviation ($n = 3$). Statistical analysis was conducted using one-way analysis of variance (ANOVA) ($n = 3$; $^*P < 0.05$; $^{**}P < 0.01$; $^{***}P < 0.001$). *P* values were estimated between a positive group and a control group in **b** and **f**. W/o, without; W/, with; ND, not detected; M_{red}, [Cp*Rh(bpy)H]$^+$. Protein structures were rendered using the PyMOL Molecular Graphics System version 2.1.1 (Schrödinger).

bpy = 2,2′-bipyridine) was used as an electron mediator[14,15] to achieve the highly regioselective reduction of NAD^+ into NADH. Linear sweep voltammograms show a cathodic current of M_{ox} in an O_2-depleted sodium phosphate (NaPi) buffer (100 mM, pH 7.5) (Fig. 2d). The addition of NAD^+ further increased the cathodic current, indicating the catalytic effect of M_{red} ([Cp*Rh(bpy)H]$^+$) in the electron transfer from CFP to NAD^+. However, the CFP cathode did not generate any cathodic current when using NAD^+ without M_{ox} (Supplementary Fig. 5), indicating the imperceptible direct reduction of NAD^+. We further confirmed the CFP-driven conversion of NAD^+ to NADH using M_{ox}; the ^1H NMR spectrum exhibited a characteristic peak at 6.94 ppm for NADH when we performed controlled potential electrolysis at −0.2 V_{RHE} (Fig. 2e and Supplementary Fig. 6). The rate of NADH production was 1.19 ± 0.07 mM h^{-1} at this electrical bias (Fig. 2f) but became negligible in the absence of M_{ox}, NAD^+ or electrical bias.

We applied the electrocatalytic regeneration system to activate GDH from bovine liver; GDH has been reported to receive electrons from NADH for the reductive amination reaction, which is a pivotal organic reaction[16] for the synthesis of amines, pharmaceuticals,

agrochemicals and biomolecules. The redox enzyme converts α-ketoglutarate to L-glutamate[17], which is a global food-flavour enhancer[18], a crop-protection agent[19] and a livestock nutrient[20]. As shown in Fig. 2g, L-glutamate was formed with a rate of $2.74 \pm 0.11\ mM\ h^{-1}$ and a TOF_{GDH} of $5{,}500 \pm 200\ h^{-1}$ at $-0.2\ V_{RHE}$; the rate of enzymatic reaction was higher than that of the NADH formation reaction (Fig. 2f), which has been observed in reports[17,21,22] on GDH catalysis driven by NADH regeneration. We can attribute this to the faster regeneration of NADH caused by NADH-consuming GDH. The omission of M_{ox}, NAD^+ or GDH resulted in a negligible amount of L-glutamate (Fig. 2g), which indicates electron transport from CFP to GDH through an NADH regeneration process. Thermal denaturation of the GDH did not result in the production of the product (Fig. 2g).

Furthermore, we revealed the general applicability of the NADH regeneration system by coupling it with OYE-driven asymmetric hydrogenation reactions. In this experiment, we used an OYE from *Thermus scotoductus* (*Ts*OYE) to catalyse the enantioselective *trans*-hydrogenation of conjugated C=C bonds[23,24]. The 2001 Nobel Prize in Chemistry award accentuated the importance of catalysed enantioselective hydrogenation reactions[14,23]. In addition, we replaced the NaPi buffer with a solution buffered using triethanolamine (TEOA)[23] (100 mM, pH 7.5; see the rationale for this alteration in the Supplementary Methods); the rate of NADH formation remained constant regardless of the electrolyte type (Supplementary Fig. 7). Controlled potential electrolysis at $-0.2\ V_{RHE}$ resulted in enzymatic conversion of 2-methyl-2-cyclohexen-1-one to (*R*)-2-methylcyclohexanone (e.e. > 99%) with a rate of $1.16 \pm 0.16\ mM\ h^{-1}$ and a TOF_{TsOYE} of $230 \pm 30\ h^{-1}$ (Fig. 2h). The rate of this enzymatic reaction was similar to that of the NADH regeneration reaction (Supplementary Fig. 7). However, the formation was rate substantially decreased when *Ts*OYE was thermally denatured (Fig. 2h) and became imperceptible with the omission of *Ts*OYE, M_{ox}, NAD^+ and the electrical bias.

Photoanodic electron extraction from microplastics. To provide electrons for the CFP-based cathodes, we chose α-Fe_2O_3 because of its abundance (Fe and O as the fourth and first most abundant elements in the Earth's crust, respectively)[25], its non-toxicity[25] and its excellent photoelectrochemical (PEC) stability under alkaline conditions (pH 13.6)[25] compared with visible-light-absorbing metal oxide semiconductors (for example, $BiVO_4$ (unstable at pH > 11)[26] and WO_3 (unstable at pH > 4)[27]). We synthesized an α-Fe_2O_3 photoelectrode by first hydrothermally depositing akaganeite (β-FeOOH) on a fluorine-doped tin oxide glass and then thermally converting β-FeOOH into worm-like α-Fe_2O_3 (90 ± 12 nm in diameter, 312 ± 91 nm in length; Fig. 3a,b). Characterization details using SEM, X-ray photoelectron spectroscopy and X-ray diffraction are shown in Fig. 3a,b and Supplementary Fig. 8. We investigated this photoelectrode's optical and electronic properties because these photophysical properties determine the PEC efficiencies. According to our ultraviolet-visible spectroscopy analysis, the α-Fe_2O_3 absorbed UV and visible light below approximately 580 nm with a bandgap of 2.00 eV (Supplementary Fig. 8f,g). From the UV photoelectron spectrum and bandgap of α-Fe_2O_3, its valence-band-edge potential and conduction-band-edge potential were estimated to be 2.52 and $0.52\ V_{RHE}$, respectively (Supplementary Fig. 8g,h).

We investigated the PEC performance of α-Fe_2O_3 on electron extraction from PET microplastics under different conditions at 303 K: (1) with no bias in the dark, (2) with an anodic bias ($1.0\ V_{RHE}$) in the dark, (3) with no bias under solar light (using an air mass 1.5 global (AM 1.5 G) solar spectrum; $100\ mW\ cm^{-2}$) and (4) with the anodic bias under solar light. Note that the PEC experiments began immediately as soon as we prepared an unpretreated PET solution ($1\ mg\ ml^{-1}$) by adding PET microplastics (size ≤ ~5 mm) to an aqueous 5 M NaOH electrolyte solution (see Methods for details). Quantitative ^1H NMR spectroscopy of the PET shows the solubilization of PET to ethylene glycol (EG) and benzene-1,4-dicarboxylate (BD) under conditions (1), (2) and (3) (Supplementary Fig. 9), which we attribute to the alkaline hydrolysis of the ester functional groups of PET. By stark contrast, the positive group—condition (4)—resulted in the formation of 530 ± 23 nmol formate and 185 ± 9 nmol acetate (Supplementary Fig. 9a). These results signify that the α-Fe_2O_3 photoanode extracts electrons and produces organic fuels from solubilized non-recyclable microplastics.

Mechanistic investigation. We performed mechanistic analyses to examine the underlying photoredox chemistry driven by α-Fe_2O_3. For the analyses, we constructed a two-compartment, three-electrode configuration using a salt bridge, which maintains electrical neutrality within the internal circuit. We confirmed that PET reformation occurs through the photo-oxidative pathway; as shown in Supplementary Fig. 10a, we detected formate and acetate at the anodic site but not at the cathodic site. Because the photoanode generated photoexcited holes, O_2, H_2O_2 and $HO^•$ (Supplementary Fig. 10b), we investigated which species drove the waste-to-chemical conversion. As shown in Fig. 3c, the addition of sodium sulfite (hole scavenger) suppressed the reaction, whereas the presence of sodium pyruvate[28] (H_2O_2 scavenger) or *tert*-butyl alcohol ($HO^•$ radical scavenger) as well as purging with N_2 gas did not restrain the formation of formate and acetate. Note that H_2O_2 and O_2 themselves do not bring about the target reaction under dark conditions without an electrical bias (Supplementary Fig. 10c). These results indicate that a photoexcited hole is responsible for the photo-oxidative reaction.

Because the alkaline solubilization of PET microplastics resulted in the formation of EG and BD (Supplementary Fig. 9b), we investigated which molecules reacted with the photoexcited holes from α-Fe_2O_3. ^1H and ^{13}C NMR spectroscopic analyses show that photoelectroactivated α-Fe_2O_3 oxidizes EG to a variety of products (Supplementary Fig. 11a,b). The oxidation products included C2 intermediates (for example, glyoxal, glycolate and glyoxylate) and C1 molecules (such as formate and acetate). These oxidation intermediates have been reported[29,30] to be formed through the oxidation reaction of EG, and further oxidized to formate and acetate under alkaline conditions. The photoactivated α-Fe_2O_3 oxidized the C2 intermediates to formate and acetate (Supplementary Fig. 11c–e). However, α-Fe_2O_3 did not oxidize BD during the PEC reaction (Supplementary Fig. 11f), which we attribute to the difficulty of oxidizing stable aromatic moieties.

We observed the dependency of the PEC oxidation rates on the applied bias and PET concentration. In the kinetic experiments, we prepared a pretreated PET solution ($5\ mg\ ml^{-1}$; see Methods for details) as an electrolyte solution; this pretreatment step solubilizes the solid wastes in advance, which facilitates contact between the photoelectrocatalyst and the substrate. Linear sweep voltammetric analysis shows that the anodic current of α-Fe_2O_3 increases with increasing applied bias and PET concentration under light conditions, but the current is negligible under dark conditions (Supplementary Fig. 12a,b). Consistent with these results, the production rate of formate and acetate increased with increasing applied bias from 0.7 to $1.2\ V_{RHE}$ and PET concentration from 0 to $10\ mg\ ml^{-1}$ (Supplementary Fig. 12c,d).

Haematite doping for enhanced photoanodic reactions. The separation of photoexcited charge carriers plays a decisive role in the efficiency of PEC reactions because it increases the concentration of charge carriers that participate in a photoredox reaction. We hypothesized that a doping treatment of α-Fe_2O_3 should boost the efficiency of the waste-to-chemical reaction because this strategy will increase the electron concentration, to enhance the electrical conductivity and suppress charge recombination, as well as making the α-Fe_2O_3 band bending upward more to provide a strong driving force for charge separation[31,32]. Thus, we introduced Zr^{4+} atoms into

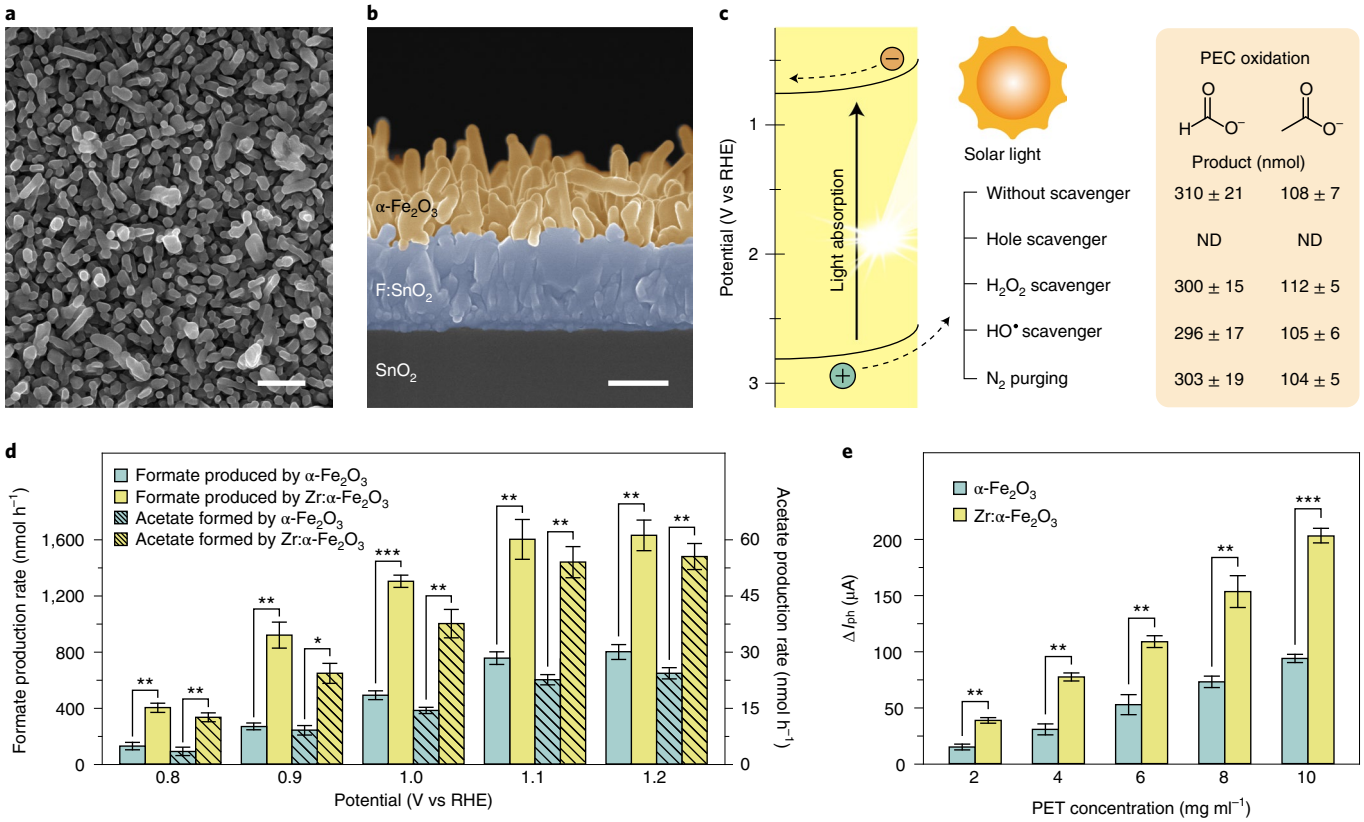

Fig. 3 | PEC reformation of PET microplastics using Fe_2O_3-based photoanodes. a, Plan-view SEM image of α-Fe_2O_3 electrode. Scale bar, 500 nm. **b**, Cross-sectional-view SEM image of the photoelectrode. Scale bar, 400 nm. **c**, Effects of various scavengers and N_2 molecules on the PEC oxidation of PET microplastics for 12 h at 1.0 V_{RHE}. Concentrations of scavengers: 300 mM sodium sulfite (hole scavenger), 300 mM sodium pyruvate (H_2O_2 scavenger) and 300 mM *tert*-butyl alcohol (HO• radical scavenger). We separated the photoanodic and cathodic sites using a salt bridge. **d**, Potential-dependent production rates of formate and acetate driven by α-Fe_2O_3 and Zr:α-Fe_2O_3 photoanodes. **e**, Comparison of ΔI_{ph} of the haematite-based photoanodes at 1.1 V_{RHE}. $\Delta I_{ph} = I_{ph}$ (at a specific PET concentration) − I_{ph} (at 0 mg ml^{-1} PET). In **c**–**e**, the light source is a solar simulator (AM 1.5 G, 100 mW cm^{-2}), the temperature is 303 K and the electrolyte solutions are unpretreated PET solution (1 mg ml^{-1} PET microplastics, 5 M NaOH) (**c**), pretreated PET solution (5 mg ml^{-1} PET microplastics, 5 M NaOH) (**d**) and pretreated PET solution (2–10 mg ml^{-1} PET microplastics, 5 M NaOH) (**e**). The error bars correspond to the standard deviation ($n = 3$). Statistical analysis was performed using one-way ANOVA ($n = 3$; $^*P < 0.05$; $^{**}P < 0.01$; $^{***}P < 0.001$). I_{ph}, photocurrent.

the α-Fe_2O_3 nanostructure to synthesize a Zr:α-Fe_2O_3 photoanode since the Zr dopants have been reported to provide electrons for α-Fe_2O_3 and, in terms of a small polaron model as a conduction mechanism,[33] accelerate electron transport between Fe atoms, which are both beneficial for increasing carrier conductivity. Doping with Zr scarcely altered the phase, morphology, optical bandgap and band-edge potentials of the photoanode (Supplementary Fig. 13).

We observed the enhanced PEC performance of the Zr:α-Fe_2O_3 photoanode. The photoanodic current of Zr:α-Fe_2O_3 increased considerably and the onset potential of water oxidation was cathodically shifted by 0.18 V when we used 2 mM Zr^{4+} ions in the precursor solution (Supplementary Fig. 14). We attribute the improved performance to an increased electron concentration (Supplementary Fig. 15a), enhanced charge-separation dynamics (Supplementary Fig. 15b), decreased charge-transfer resistance at the Zr:α-Fe_2O_3 interface (Supplementary Fig. 15c,d), suppressed charge recombination (Supplementary Fig. 16) and more upward band bending (Supplementary Fig. 15a), which we obtained using (transient) voltammetric analysis, Mott–Schottky analysis and electrochemical impedance spectroscopy. Detailed analytical results are shown in Supplementary Figs. 15 and 16.

These photophysical improvements caused by Zr doping resulted in faster PET reformation. Figure 3d shows that Zr:α-Fe_2O_3 exhibits a faster production of formate and acetate than the α-Fe_2O_3 photoanode from 0.8 to 1.2 V_{RHE}. Consistent with these results, the Zr:α-Fe_2O_3 photoanode generated a higher photoanodic current than did α-Fe_2O_3 under the same PET concentrations (Fig. 3e), which is beneficial for faster electron transport to CFP-based cathodes for rapid biocatalytic reactions. Furthermore, the Zr:α-Fe_2O_3 electrode exhibited negligible PEC decomposition of formate and acetate from 0.8 to 1.2 V_{RHE} (Supplementary Fig. 17 and Supplementary Table 2).

We confirmed the robust PEC stability of Zr:α-Fe_2O_3. As shown in Supplementary Fig. 18, Zr:α-Fe_2O_3 exhibited a steady formation rate of formate and acetate during a seven-iteration experiment (a 12 h reaction per cycle). In addition, the phase and surface chemical states of Zr:α-Fe_2O_3 did not alter (Supplementary Fig. 19 and Supplementary Table 3) and its constituent atoms did not leak into the electrolyte solution after the reusability test (Supplementary Table 4). These results indicate the suitability of Zr:α-Fe_2O_3 for long-term PEC reactions.

Furthermore, we revealed the real-world applicability of the Zr:α-Fe_2O_3 energy material using microplastics from post-consumer PET waste, including a PET disposable cup and a PET bottle. The application of solar energy (1 sun) and electrical bias (1.1 V_{RHE}) to the photoanode triggered the formation of approximately 1.7 mmol formate and 40 μmol acetate from an unprehydrolysed PET cup and a PET bottle for 10 days (Supplementary Fig. 20).

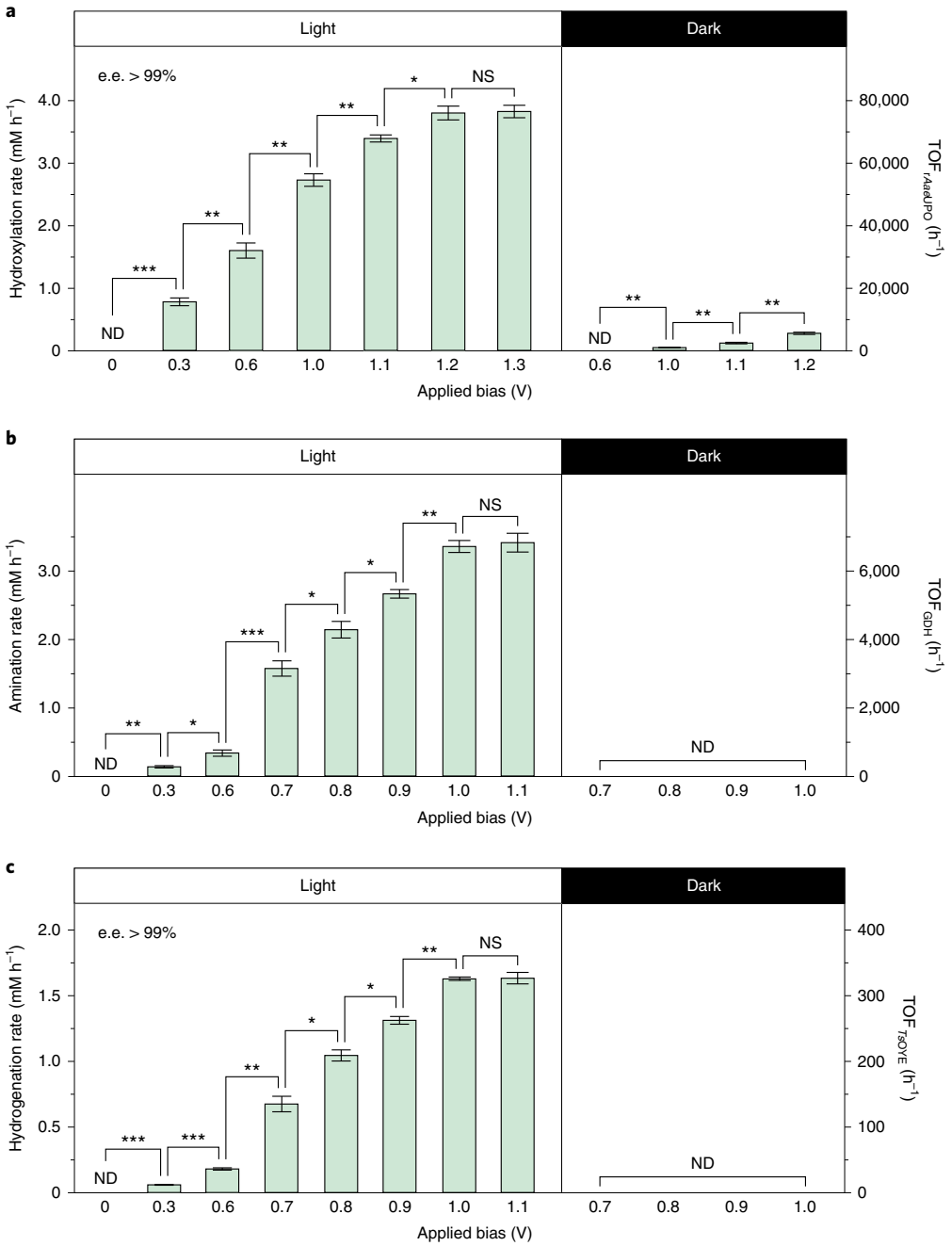

Fig. 4 | BPEC synthesis using real-world microplastics. a–c, Solar-powered enzymatic reactions driven by r*Aae*UPO (**a**), GDH (**b**) and *Ts*OYE (**c**). Cathodic electrolyte: 50 nM r*Aae*UPO and 16 mM ethylbenzene in an O_2-rich KPi buffer (100 mM, pH 6.0) (**a**); 500 nM GDH, 80 mM α-ketoglutarate, 250 mM NH_4^+, 0.25 mM M_{ox} and 1 mM NAD^+ in an O_2-depleted NaPi buffer (100 mM, pH 7.5) (**b**); 5 μM *Ts*OYE, 7 mM 2-methyl-2-cyclohexen-1-one, 10 mM $CaCl_2$, 20 mM NH_4^+, 0.25 mM M_{ox} and 1 mM NAD^+ in an O_2-depleted TEOA-buffered solution (100 mM, pH 7.5) (**c**). Cathode: AQC/CFP electrode (**a**); CFP electrode (**b**,**c**). In **a**–**c**, the anodic electrolyte was pretreated PET solution (50 mg ml^{-1} PET microplastics, 5 M NaOH) using post-consumer PET disposable cups, the temperature was 303 K and the light conditions were 1 sun illumination (AM 1.5 G, 100 mW cm^{-2}). We irradiated solar light onto the anodic site, not the cathodic site. The error bars correspond to the standard deviation ($n = 3$). Statistical analysis was performed using one-way ANOVA ($n = 3$; $^*P < 0.05$; $^{**}P < 0.01$; $^{***}P < 0.001$; NS, not significant).

Photobiosynthesis fuelled by post-consumer microplastics. Having substantiated CFP-mediated biosynthetic reactions and Zr:α-Fe_2O_3-driven transformation reactions, we integrated these two redox reactions in a two-compartment, two-electrode configuration (working electrode, Zr:α-Fe_2O_3 photoanode; counter electrode, AQC/CFP or CFP cathode). We prepared a pretreated PET solution—using microplastics from a post-consumer PET disposable cup—as an anodic electrolyte solution. Controlled potential photoelectrolysis triggered biocatalytic synthesis, including the r*Aae*UPO-driven formation of enantiopure (*R*)-1-phenylethanol, the GDH-driven production of L-glutamate and the *Ts*OYE-catalysed generation of enantiopure (*R*)-2-methylcyclohexanone (Fig. 4 and Supplementary Figs. 21 and 22). The enantioselectivities remained constant (e.e. > 99%) regardless of the size of the applied bias (Fig. 4a,c). Shielding the PEC system from solar light made the synthetic reactions sluggish or imperceptible (Fig. 4), signifying that

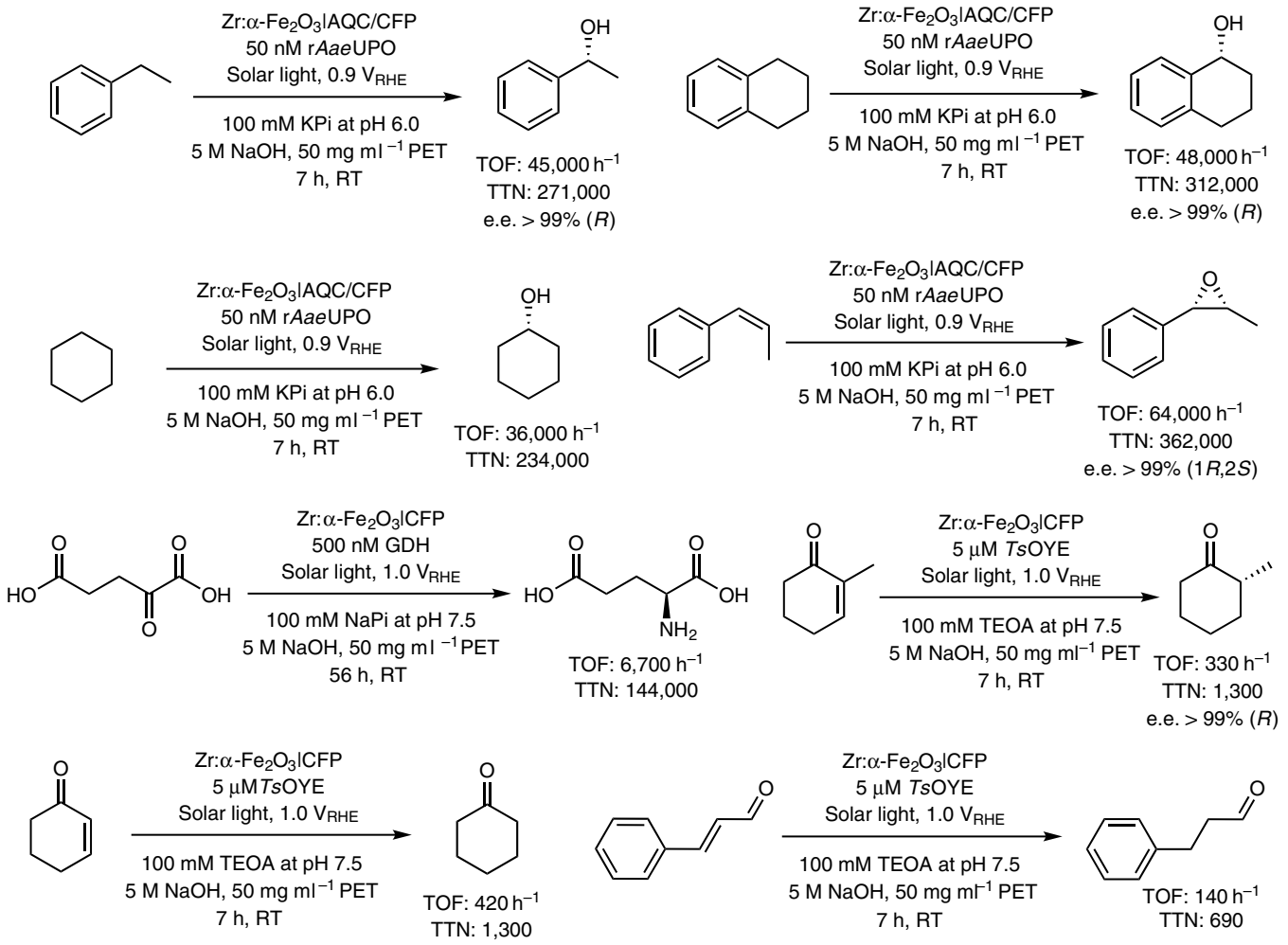

Fig. 5 | Substrate scope of BPEC reactions using real-world PET microplastics. Cathodic electrolyte for r*Aae*UPO reactions, including the enantioselective hydroxylation of ethylbenzene, tetralin and cyclohexane as well as the epoxidation of *cis*-β-methylstyrene: 50 nM r*Aae*UPO and 16 mM substrate in an O_2-rich KPi buffer (100 mM, pH 6.0). Cathodic electrolyte for GDH-driven reductive amination of α-ketoglutarate: 500 nM GDH, 80 mM α-ketoglutarate, 250 mM NH_4^+, 0.25 mM M_{ox} and 1 mM NAD^+ in an O_2-depleted NaPi buffer (100 mM, pH 7.5). Cathodic electrolyte for *Ts*OYE-driven hydrogenation of 2-methyl-2-cyclohexen-1-one, 2-cyclohexen-1-one and *trans*-3-phenyl-2-propenal: 5 μM *Ts*OYE, 7 mM substrate, 10 mM $CaCl_2$, 20 mM NH_4^+, 0.25 mM M_{ox} and 1 mM NAD^+ in an O_2-depleted TEOA-buffered solution (100 mM, pH 7.5). Anodic electrolyte: pretreated PET solution (50 mg ml^{-1} PET microplastics, 5 M NaOH) using real-world PET disposable cups. Light conditions: 1 sun illumination (AM 1.5 G, 100 mW cm^{-2}). RT, room temperature (303 K).

solar energy is a key energy resource for driving the redox reactions at a meaningful rate. We also revealed that the rates of the photobiosynthetic reactions increased with the PET concentration from 0 to 50 mg ml^{-1} (Supplementary Fig. 23), which indicates that PET provides electron donors (for example, EG) for boosting enzymatic transformation reactions.

Using the optimized applied bias of each enzymatic reaction, our photobiocatalytic system exhibited a $TTN_{rAaeUPO}$ of 113,000 (3 h), a TTN_{GDH} of 144,000 (56 h) and a TTN_{TsOYE} of 1,300 (7 h) (Fig. 5 and Supplementary Fig. 24a). The reaction times of GDH and *Ts*OYE were longer than those reported in previous research on BPEC systems[17,34–36], which we attribute to the robustness of the Zr:α-Fe_2O_3|CFP system and the biocatalysts. However, the r*Aae*-UPO reaction halted at around 2 h (Supplementary Fig. 24a), which was shorter than that recorded in a previous BPEC study[37]. We found that the CFP cathode formed HO• radicals (Supplementary Fig. 24b), which have been reported[37,38] to be capable of deactivating the enzyme. Because electrochemical reduction of H_2O_2 forms HO• radicals[39], we decreased the applied bias from 1.2 to 0.9 V_{RHE}, which resulted in negligible formation of the radicals (Supplementary Fig. 24b). This strategy resulted in a steady biosynthetic reaction with a $TTN_{rAaeUPO}$ of 271,000 (7 h) (Fig. 5 and Supplementary Fig. 24a). Zr:α-Fe_2O_3 produced formate and acetate during the PEC reactions (Supplementary Table 5), which indicates the production of value-added compounds simultaneously at the anodic and cathodic sites.

We demonstrated the broad applicability of the photobiosynthetic platform by extending the substrate scope (Supplementary Table 6). Figure 5 and Supplementary Fig. 22 display the r*Aae*UPO-mediated synthesis of (*R*)-1,2,3,4-tetrahydro-1-naphthol (e.e. > 99%, TOF = 48,000 h^{-1}, TTN = 312,000), cyclohexanol (TOF = 36,000 h^{-1}, TTN = 234,000) and (1*R*,2*S*)-1-phenylpropylene oxide (e.e. > 99%, TOF = 64,000 h^{-1}, TTN = 362,000), as well as the *Ts*OYE-driven production of cyclohexanone (TOF = 420 h^{-1}, TTN = 1,300) and 3-phenylpropionaldehyde (TOF = 140 h^{-1}, TTN = 690).

Discussion

Inspired by natural photosynthesis, BPEC platforms synthesize value-added compounds through the cooperation of photoelectrocatalysis with redox biotransformations[40–42]. Mechanistically, a photoelectrode absorbs solar energy and transfers its photoexcited

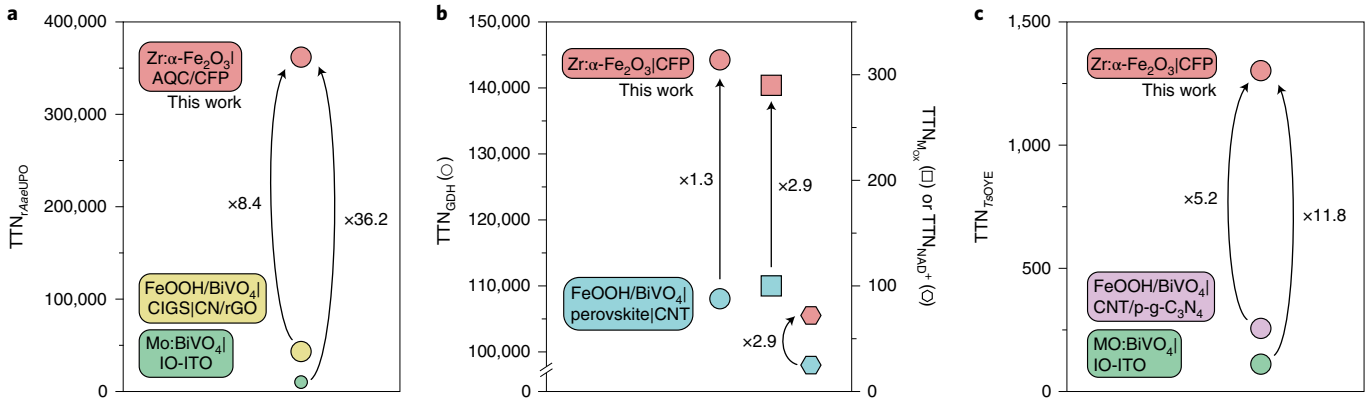

Fig. 6 | Synthetic efficiencies of oxidoreductases in state-of-the-art BPEC systems. a–c, Redox enzymes' TTNs for photobiosyntheses activated by r*Aae*UPO[36,37] (**a**), GDH[17] (**b**) and *Ts*OYE[35,36] (**c**). Assembly: FeOOH/$BiVO_4$|CIGS|CN/rGO (yellow; ref. [37]), Mo:$BiVO_4$|IO-ITO (green; ref. [36]), FeOOH/$BiVO_4$|perovskite|CNT (cyan; ref. [17]), FeOOH/$BiVO_4$|CNT/p-g-C_3N_4 (purple; ref. [35]). FeOOH/$BiVO_4$, FeOOH-deposited $BiVO_4$; CIGS, Cu(In,Ga)Se_2; CN/rGO, graphitic carbon nitride/reduced graphene oxide hybrid; Mo:$BiVO_4$, Mo-doped $BiVO_4$; IO-ITO, inverse opal-structured indium tin oxide; CNT, carbon nanotube film; CNT/p-g-C_3N_4, carbon nanotube/protonated graphitic carbon nitride hybrid.

charge carriers to the catalytic centre of redox enzymes, which subsequently catalyse synthetically useful redox reactions (for example, asymmetric hydrogenation of C=C bonds, amination of C=O bonds, hydroxylation of C–H bonds and epoxidation of C–H bonds)[14]. Traditional PEC cells are classified into regenerative and photosynthetic cells, in which semiconducting electrodes directly convert sunlight into, respectively, electric power or chemical fuels (for example, H_2)[43]. By contrast, BPEC approaches develop new concepts[14,44] for solar-energy conversion using solid-state catalytic electrodes as solar-powered activators of oxidoreductases[45] (Supplementary Table 7); the biocatalytic components perform organic synthetic reactions that (semi)conductors generally cannot perform with excellent chemo-, regio- and stereoselectivities, high catalytic efficiencies and environmental benignity.

The BPEC system has emerged as an alternative platform to the biocatalytic photocatalytic (BPC) system. These two approaches harvest clean and abundant solar energy to generate photoexcited charge carriers for driving enzymatic reactions (Supplementary Table 8). BPC systems, using molecular[46–48] or semiconducting photocatalysts[49,50], can have the advantage that catalytic reactions take place throughout the reaction medium without mass-transfer limitations. However, compared with BPEC approaches, many BPC systems suffer from the recombination[14,45] of photoexcited charge carriers and cannot use the merits that originate from the separation of oxidation and reduction sites (such as the preservation of redox enzymes from reactive oxidized electron donors[45]). In contrast to these light-driven routes, bioelectrocatalytic systems use electrical energy and conducting electrodes[51,52] to activate redox enzymes. Compared with BPC approaches, bioelectrocatalytic platforms have the benefit of controlling the Fermi level[14] of the catalytic electrode and driving the redox reaction selectively; however, bioelectrocatalytic approaches suffer from mass-transport limitations[52,53] because catalytic reactions occur at the electrode/electrolyte interface. Bioelectrocatalytic and BPEC systems share the common advantages of isolating the anodic from the cathodic sites in a two-compartment configuration. However, bioelectrocatalytic approaches demand a larger electrical bias than BPEC platforms because the latter harness solar energy to generate excited electronic potentials.

The majority of BPEC systems[17,35,37,40,41] have focused on water oxidation to provide the reducing equivalents needed to drive reductive enzymatic reactions. However, water oxidation poses substantial limitations, such as its sluggish reaction rate caused by anodic four-electron (or two-electron) process[23] and the relatively low value of dioxygen[54]. This issue made us hypothesize that finding another electron feedstock would accelerate enzymatic synthetic reactions and produce value-added chemicals simultaneously on oxidation and reduction sites.

The current work demonstrates that real-world microplastics can provide electron feedstocks to expedite photobiosynthetic reactions with excellent TTNs. The two-compartment BPEC system provides several distinct advantages that are impossible in BPC processes (Supplementary Fig. 25). First, the protection of reduced mediators (such as M_{red} and NADH) and enzymes from photooxidation. Second, the flexible combination of redox reactions (for example, EG oxidation with H_2O_2 production and NADH regeneration) with different reaction conditions (such as KPi buffer (pH 6.0) with NaOH alkaline solution). Third, control of the applied bias to drive redox reactions selectively (for example, H_2O_2 production and suppressed HO• generation). Fourth, the spatial separation of enzymatic products (such as (*R*)-1-phenylethanol, L-glutamate and (*R*)-2-methylcyclohexanone) and oxidation products (such as formate and acetate). Fifth, the development of individual (photo)electrodes (for example, Zr:α-Fe_2O_3 and AQC/CFP). Sixth, the facile reusability of catalytic electrodes.

Our BPEC platform compares favourably with state-of-the-art BPEC systems in a two-electrode configuration (Fig. 6). The reported PEC cells[17,35–37] extracted electrons from water to trigger redox biotransformations driven by r*Aae*UPO ($TTN_{rAaeUPO} \leq 43{,}000$)[36,37], GDH ($TTN_{GDH} = 108{,}000$)[17] or *Ts*OYE ($TTN_{TsOYE} \leq 250$)[35,36]. Our PEC system acquired electrons from hydrolysed PET solutions and accelerated enzymatic synthetic reactions with the highest TTN_{enzyme} values ($TTN_{rAaeUPO} = 362{,}000$, $TTN_{GDH} = 144{,}000$, $TTN_{TsOYE} = 1{,}300$) among solar-driven BPEC systems (Supplementary Table 9). Furthermore, the Zr:α-Fe_2O_3 photoanode exhibits a higher production rate of formate (μmol per cm^2 anode per h per g PET) than the reported catalytic anode[55] (Supplementary Table 10). This performance could be the result of the poor decomposition of formate and acetate driven by the Zr:α-Fe_2O_3 photoanode. We suspect that formate and acetate may undergo poor adsorption and oxidation at the surface of Zr:α-Fe_2O_3, as reported in the literature[56,57], for the α-Fe_2O_3-driven PEC oxidation of organic molecules.

Follow-up studies are needed to improve the photoanodic performance of electron extraction through, for example, the demonstration of detailed PEC mechanisms of PET reformation by Zr:α-Fe_2O_3, modification of the surface morphology to decrease charge recombination, and construction of junctions to improve

charge separation. In addition, functionalization of cathodes with additional catalysts would accelerate enzymatic reactions by boosting interfacial charge transfer to enzyme activators. These studies will further expand the scope of our approach to other redox enzymatic reactions (for example, hydrogenase-driven evolution of H_2 as well as Baeyer–Villiger monooxygenase-mediated formation of esters and lactones) with improved efficiencies.

This study reports a solar-assisted e-biorefinery approach that uses PET microplastics as an electron feedstock for redox biosynthesis. The Zr:α-Fe_2O_3|AQC/CFP and Zr:α-Fe_2O_3|CFP hybrids produced value-added chemicals at the anodic and cathodic sites through simultaneous enzymatic synthetic reactions (r*Aae*UPO-driven hydroxylation/epoxidation, GDH-mediated amination and *Ts*OYE-catalysed hydrogenation) as well as EG oxidation. The photoanodic half-reaction by α-Fe_2O_3 led to delivery of electrons to the CFP-based cathode and the generation of valuable chemicals (for example, formate and acetate). To accelerate the photoanodic extraction of electrons, we synthesized the Zr:α-Fe_2O_3 photoanode that exhibited improved charge-separation efficiencies ($\Delta\eta_{bulk}$ of 3.5–10%, $\Delta\eta_{surface}$ of 15–60%), a decreased charge-transfer resistance (by up to 17 times), a cathodic shift of the flat-band potential by 0.16 V and reduced charge-recombination behaviour. Furthermore, the Zr:α-Fe_2O_3 photoanode reformed real-world PET items for over ten days. This microplastic-fuelled PEC biocatalysis showed a broad applicability to various enzymatic substrates and achieved benchmark performances ($TTN_{rAaeUPO}$ = 362,000, TTN_{GDH} = 144,000 and TTN_{TsOYE} = 1,300).

Methods

Characterization of CFP. We bought a commercial CFP from HanTech. Before performing any experiments, we washed the CFP using deionized water, ethanol and acetone, and then dried it under vacuum at room temperature. We used an ultrahigh-resolution scanning electron microscope SU8230 (Hitachi High-Tech) to observe the morphology of the CFP. We used a K-Alpha X-ray photoelectron spectrometer (ThermoFisher Scientific) to investigate chemical states of the CFP. We obtained the Raman spectrum of CFP using a LabRAM HR Evolution Raman microscope (Horiba) with an excitation wavelength of 514 nm.

Preparation of AQC/CFP cathode. We purified commercial CFP as mentioned above. To prepare AQC/CFP, we immersed the CFP in an ethanolic solution containing 3 mM AQC for 24 h. Subsequently, we dried it at room temperature in air. We estimated the amount of surface-bound AQC using cyclic voltammetric analysis; the surface concentration of AQC (Γ_{AQC}) was estimated using equation (1)

$$\Gamma_{AQC}\left(\text{nmol cm}^{-2}\right) = Q \times (n \times F \times A)^{-1} \quad (1)$$

where Q is the charge consumed for the reduction of AQC, which was calculated from a cyclic voltammogram of AQC/CFP, n is the number of electrons transferred to AQC (n = 2), F is the Faraday constant (96,485 C mol^{-1}), and A is the geometrical surface area of the CFP. We obtained Nyquist plots of the CFP and AQC/CFP electrodes using a ZIVE SP1 impedance analyser (WonATech) at an alternating-current potential amplitude of 10 mV. We fitted the Nyquist plots to calculate their charge-transfer resistance values using ZMAN software (WonATech).

Electrocatalytic production of H_2O_2. Electrocatalytic production of H_2O_2 was performed using a three-electrode configuration (reference electrode: Ag/AgCl (3 M NaCl)). The electrolyte solution was a KPi buffer (100 mM, pH 6.0). When we applied an electrical bias to this system, we used a WMPG 1000 potentiostat/galvanostat (WonATech). When we investigated the pathway of the electrochemical production of H_2O_2, we added 10 mM 1,4-benzoquinone ($O_2^{\bullet-}$ scavenger) to the electrolyte solution. All potentials are quoted versus the RHE according to equation (2).

$$E_{RHE}\,(\text{V}) = E_{Ag/AgCl}\,(\text{V}) + 0.209 + (0.059 \times \text{pH}) \quad (2)$$

After the electrochemical reaction, we collected the reaction solution and mixed it with a colorimetric reagent solution (3.0 U horseradish peroxidase and 2 mM 2,2′-azino-bis(3-ethylbenzothiazoline-6-sulfonic acid) in a KPi solution (100 mM, pH 5.0)). We monitored its absorbance at 420 nm using a V-650 UV-visible absorption spectrophotometer (JASCO).

Bioelectrocatalytic oxyfunctionalization reactions. We applied AQC/CFP-driven H_2O_2 production to r*Aae*UPO-mediated oxyfunctionalization reactions using a one-compartment, three-electrode configuration. The reference electrode was Ag/AgCl (3 M NaCl). The electrolyte solution was an O_2-rich KPi buffer (100 mM, pH 6.0) that contained r*Aae*UPO and ethylbenzene. After the bioelectrocatalytic reaction, we extracted the oxyfunctionalized products using ethyl acetate, dried them over $MgSO_4$, and quantified them using a 7890A gas chromatograph (Agilent Technologies) equipped with a flame ionization detector and a CP-Chirasil-Dex CB column (25 m × 0.32 mm × 0.25 µm).

Electrocatalytic regeneration of NADH. To investigate the capability of CFP for reducing NAD^+ to NADH, we immersed a CFP electrode in NaPi buffer (100 mM, pH 7.5) containing NAD^+ and M_{ox} using a three-electrode configuration. We used the WMPG 1000 potentiostat/galvanostat to perform electrocatalytic analysis and controlled potential electrolysis. We quantified NADH using the V-650 UV-visible absorption spectrophotometer. NMR analysis was performed to confirm the formation of NADH. We used a 400 MHz AVANCE III HD NanoBay (Bruker) spectrometer equipped with a 5 mm multinuclear broadband fluorine observe (or BBFO) probe.

Bioelectrocatalytic amination and hydrogenation. To carry out enzymatic amination reactions, we dissolved GDH, α-ketoglutarate, NH_4^+, M_{ox} and NAD^+ in O_2-depleted NaPi buffer (100 mM, pH 7.5). The concentrations of α-ketoglutarate and L-glutamate were measured using HPLC (1260 Infinity LC System, Agilent Technologies) equipped with a variable-wavelength detector and an Intersil C18 column. To drive the enzymatic hydrogenation reactions, we added *Ts*OYE, 2-methyl-2-cyclohexen-1-one, $CaCl_2$, NH_4^+, M_{ox} and NAD^+ to O_2-depleted TEOA-buffered solution (100 mM, pH 7.5). The products of *Ts*OYE were quantified using the 7890A gas chromatograph equipped with a flame ionization detector and a CP-Chirasil-Dex CB column (25 m × 0.32 mm × 0.25 µm).

Fabrication of photoanodes. We synthesized a haematite photoanode via solution-based processing and high-temperature annealing. A commercial fluorine-doped tin oxide glass (F:SnO_2; TEC-7, Pilkington) was rinsed with acetone, isopropyl alcohol and deionized water. To deposit a β-FeOOH nanostructure on the F:SnO_2 substrate, we prepared a precursor solution containing 150 mM $FeCl_3{\cdot}6H_2O$ and 1 M $NaNO_3$ in deionized water. The substrate was immersed in the solution and heated using a Lindberg/Blue M muffle furnace (Fisher Scientific) at 100 °C. To transform β-FeOOH into α-Fe_2O_3, the electrode was annealed at 800 °C. When we prepared the Zr:α-Fe_2O_3, we added $ZrCl_4$ to the precursor solution and followed the above-mentioned method.

Preparation of PET-containing electrolyte solutions. Granular PET polymer (Sigma-Aldrich) and commercial PET items were ground to microplastics (size ≤ ~5 mm) using a commercial coffee grinder. After we had prepared an electrolyte solution by adding the microplastics to 5 M NaOH solution, we immediately conducted the photoelectrocatalytic reactions unless otherwise specified. We designated the solution as 'unpretreated PET solution', and its concentration details are given in the main text and figures. To prepare a 'pretreated PET solution', we immersed the microplastics in 5 M NaOH solution at 353 K under dark conditions with stirring at 700 revolutions per minute unless otherwise specified; the amount of microplastic is mentioned in the main text and figures.

Photoelectrochemical reformation of PET. We performed controlled potential photoelectrolysis to drive the PEC reformation of PET. The light source was a xenon arc lamp (Newport Corporation), and the electrical bias was provided using the WMPG 1000 potentiostat/galvanostat. All potentials are quoted versus the RHE according to equation (3).

$$E_{RHE}\,(\text{V}) = E_{Hg/HgO}\,(\text{V}) + 0.140 + (0.059 \times \text{pH}) \quad (3)$$

To investigate which species (for example, holes, H_2O_2 or HO•) performed the waste-to-chemical conversion, we separated the photoanodic and cathodic sites and added sodium sulfite (hole scavenger), sodium pyruvate (H_2O_2 scavenger) or *tert*-butyl alcohol (HO• scavenger) to an unpretreated PET solution (1 mg ml^{-1} PET microplastics, 5 M NaOH). To test the effect of O_2 on the PET reformation reaction, we purged N_2 gas into the anodic electrolyte solution before and during the PEC reactions.

Quantitative NMR spectroscopy. ^{1}H NMR spectra were recorded using the 400 MHz AVANCE III HD NanoBay spectrometer equipped with a 5 mm multinuclear BBFO probe. We prepared NMR samples (700 µl) by diluting the reaction sample in D_2O solvent (v/v, 9:1) that contained maleic acid (quantification standard) and sodium trimethylsilylpropanesulfonate (chemical shift standard); D_2O was used to provide an internal lock signal to correct drift in the magnetic field during the measurements. The NMR pulse sequence, relaxation delay and temperature were zgesfpgp, 6 s and 298 K, respectively. The molar concentration of the analyte ($C_{analyte}$) in the sample was calculated according to equation (4)

$$C_{analyte} = \frac{I_{analyte} \times N_{standard}}{I_{standard} \times N_{analyte}} \times C_{standard} \quad (4)$$

where $I_{analyte}$ is the integral of the analyte peak, $I_{standard}$ is the integral of the standard peak, $N_{analyte}$ is the number of protons corresponding to the analyte peak and $N_{standard}$ is the number of protons corresponding to the standard peak.

Photoelectrochemical biocatalysis. We connected a Zr:α-Fe_2O_3 photoanode and a CFP (or AQC/CFP) cathode using a two-compartment configuration. We performed controlled potential photoelectrolysis using the xenon lamp and WMPG 1000 potentiostat/galvanostat; the experimental design was for solar light to be irradiated onto the anodic site, not the cathodic site. The geometrical surface area of the photoanode and the cathode was 1.7 and 1 cm^2, respectively, unless otherwise specified. The anodic electrolyte was a 5 M NaOH aqueous solution containing prehydrolysed PET microplastics; we prepared the microplastics by grinding post-consumer PET cups. The cathodic electrolyte was different according to the type of enzyme: for example, O_2-enriched KPi buffer (100 mM, pH 6.0) containing r*Aae*UPO and substrate for the oxyfunctionalization reactions, O_2-depleted NaPi buffer (100 mM, pH 7.5) containing GDH, α-ketoglutarate, NH_4^+, M_{ox} and NAD^+ for the amination reactions, and O_2-depleted TEOA buffer (100 mM, pH 7.5) containing *Ts*OYE, substrate, Ca^{2+}, NH_4^+, M_{ox} and NAD^+ for the hydrogenation reactions. Gas chromatographic analysis was used to quantify the enzymatic products. We calculated the TTNs of r*Aae*UPO, GDH and *Ts*OYE according to, respectively, equations (5), (6) and (7).

$$\mathrm{TTN}_{r\mathit{Aae}\mathrm{UPO}} = \frac{\text{Maximum product concentration during enzymatic reaction}}{\text{Concentration of r}\mathit{Aae}\text{UPO}} \quad (5)$$

$$\mathrm{TTN}_{\mathrm{GDH}} = \frac{\text{Maximum product concentration during enzymatic reaction}}{\text{Concentration of GDH}} \quad (6)$$

$$\mathrm{TTN}_{\mathit{Ts}\mathrm{OYE}} = \frac{\text{Maximum product concentration during enzymatic reaction}}{\text{Concentration of }\mathit{Ts}\text{OYE}} \quad (7)$$

Data availability

The data supporting the findings of the study are available in the paper and its Supplementary Information. Source data are provided with this paper.

Received: 1 February 2022; Accepted: 22 July 2022;
Published online: 12 September 2022

References

1. Ryberg, M. W., Laurent, A. & Hauschild, M. *Mapping of Global Plastics Value Chain and Plastics Losses to the Environment* (United Nations Environment Programme, 2018).
2. Adyel, T. M. Accumulation of plastic waste during COVID-19. *Science* **369**, 1314–1315 (2020).
3. Garcia, J. M. & Robertson, M. L. The future of plastics recycling. *Science* **358**, 870–872 (2017).
4. MacArthur, E. Beyond plastic waste. *Science* **358**, 843–843 (2017).
5. Ryan, P. G. in *Marine Anthropogenic Litter* (eds Bergmann, M. et al.) 1–25 (Springer, 2015).
6. Law, K. L. & Thompson, R. C. Microplastics in the seas. *Science* **345**, 144–145 (2014).
7. *The New Plastics Economy – Rethinking the Future of Plastics* (World Economic Forum, Ellen MacArthur Foundation and McKinsey & Company, 2016).
8. Singh, A. K., Yasri, N., Karan, K. & Roberts, E. P. L. Electrocatalytic activity of functionalized carbon paper electrodes and their correlation to the Fermi level derived from Raman spectra. *ACS Appl. Energy Mater.* **2**, 2324–2336 (2019).
9. Molina-Espeja, P., Ma, S., Mate, D. M., Ludwig, R. & Alcalde, M. Tandem-yeast expression system for engineering and producing unspecific peroxygenase. *Enzyme Microb. Technol.* **73–74**, 29–33 (2015).
10. Pognon, G., Brousse, T., Demarconnay, L. & Bélanger, D. Performance and stability of electrochemical capacitor based on anthraquinone modified activated carbon. *J. Power Sources* **196**, 4117–4122 (2011).
11. Zhang, W. et al. Selective aerobic oxidation reactions using a combination of photocatalytic water oxidation and enzymatic oxyfunctionalizations. *Nat. Catal.* **1**, 55–62 (2018).
12. Yoon, J. et al. Piezobiocatalysis: ultrasound-driven enzymatic oxyfunctionalization of C–H bonds. *ACS Catal.* **10**, 5236–5242 (2020).
13. Kim, J., Nguyen, T. V. T., Kim, Y. H., Hollmann, F. & Park, C. B. Lignin as a multifunctional photocatalyst for solar-powered biocatalytic oxyfunctionalization of C–H bonds. *Nat. Synth.* **1**, 217–226 (2022).
14. Kim, J. & Park, C. B. Shedding light on biocatalysis: photoelectrochemical platforms for solar-driven biotransformation. *Curr. Opin. Chem. Biol.* **49**, 122–129 (2019).
15. Ko, J. W. et al. Self-assembled peptide–carbon nitride hydrogel as a light-responsive scaffold material. *Biomacromolecules* **18**, 3551–3556 (2017).
16. Murugesan, K. et al. Catalytic reductive aminations using molecular hydrogen for synthesis of different kinds of amines. *Chem. Soc. Rev.* **49**, 6273–6328 (2020).
17. Lee, Y. W. et al. Unbiased biocatalytic solar-to-chemical conversion by FeOOH/$BiVO_4$/perovskite tandem structure. *Nat. Commun.* **9**, 4208 (2018).
18. Chaudhari, N., Landin, A. M. & Roper, S. D. A metabotropic glutamate receptor variant functions as a taste receptor. *Nat. Neurosci.* **3**, 113–119 (2000).
19. Sun, C. et al. L-Glutamate treatment enhances disease resistance of tomato fruit by inducing the expression of glutamate receptors and the accumulation of amino acids. *Food Chem.* **293**, 263–270 (2019).
20. Hou, Y. & Wu, G. L-Glutamate nutrition and metabolism in swine. *Amino Acids* **50**, 1497–1510 (2018).
21. Wang, D. et al. Lignin-fueled photoelectrochemical platform for light-driven redox biotransformation. *Green Chem.* **22**, 5151–5160 (2020).
22. Son, E. J., Lee, Y. W., Ko, J. W. & Park, C. B. Amorphous carbon nitride as a robust photocatalyst for biocatalytic solar-to-chemical conversion. *ACS Sustain. Chem. Eng.* **7**, 2545–2552 (2019).
23. Kim, J. et al. Nicotinamide adenine dinucleotide as a photocatalyst. *Sci. Adv.* **5**, eaax0501 (2019).
24. Mifsud, M. et al. Photobiocatalytic chemistry of oxidoreductases using water as the electron donor. *Nat. Commun.* **5**, 3145 (2014).
25. Shen, S., Lindley, S. A., Chen, X. & Zhang, J. Z. Hematite heterostructures for photoelectrochemical water splitting: rational materials design and charge carrier dynamics. *Energy Environ. Sci.* **9**, 2744–2775 (2016).
26. Kim, J. H. & Lee, J. S. Elaborately modified $BiVO_4$ photoanodes for solar water splitting. *Adv. Mater.* **31**, 1806938 (2019).
27. Liu, X., Wang, F. & Wang, Q. Nanostructure-based WO_3 photoanodes for photoelectrochemical water splitting. *Phys. Chem. Chem. Phys.* **14**, 7894–7911 (2012).
28. Heo, Y., Kim, K., Kim, J., Jang, J. & Park, C. B. Near-infrared-active copper bismuth oxide electrodes for targeted dissociation of Alzheimer's β-amyloid aggregates. *ACS Appl. Mater. Interfaces* **12**, 23667–23676 (2020).
29. Uekert, T., Kasap, H. & Reisner, E. Photoreforming of nonrecyclable plastic waste over a carbon nitride/nickel phosphide catalyst. *J. Am. Chem. Soc.* **141**, 15201–15210 (2019).
30. Uekert, T., Kuehnel, M. F., Wakerley, D. W. & Reisner, E. Plastic waste as a feedstock for solar-driven H_2 generation. *Energy Environ. Sci.* **11**, 2853–2857 (2018).
31. Iandolo, B., Wickman, B., Zorić, I. & Hellman, A. The rise of hematite: origin and strategies to reduce the high onset potential for the oxygen evolution reaction. *J. Mater. Chem. A* **3**, 16896–16912 (2015).
32. Xiao, M., Luo, B., Wang, Z., Wang, S. & Wang, L. Recent advances of metal-oxide photoanodes: engineering of charge separation and transportation toward efficient solar water splitting. *Sol. RRL* **4**, 1900509 (2020).
33. Liao, P., Toroker, M. C. & Carter, E. A. Electron transport in pure and doped hematite. *Nano Lett.* **11**, 1775–1781 (2011).
34. Nam, D. H. et al. Water oxidation-coupled, photoelectrochemical redox biocatalysis toward mimicking natural photosynthesis. *Appl. Catal. B* **198**, 311–317 (2016).
35. Son, E. J. et al. Carbon nanotube–graphitic carbon nitride hybrid films for flavoenzyme-catalyzed photoelectrochemical cells. *Adv. Funct. Mater.* **28**, 1705232 (2018).
36. Choi, D. S., Kim, J., Hollmann, F. & Park, C. B. Solar-assisted eBiorefinery: photoelectrochemical pairing of oxyfunctionalization and hydrogenation reactions. *Angew. Chem. Int. Ed.* **59**, 15886–15890 (2020).
37. Choi, D. S. et al. Bias-free in situ H_2O_2 generation in a photovoltaic–photoelectrochemical tandem cell for biocatalytic oxyfunctionalization. *ACS Catal.* **9**, 10562–10566 (2019).
38. Burek, B. O. et al. Photoenzymatic hydroxylation of ethylbenzene catalyzed by unspecific peroxygenase: origin of enzyme inactivation and the impact of light intensity and temperature. *ChemCatChem* **11**, 3093–3100 (2019).
39. Perry, S. C. et al. Electrochemical synthesis of hydrogen peroxide from water and oxygen. *Nat. Rev. Chem.* **3**, 442–458 (2019).
40. Kuk, S. K. et al. CO_2-reductive, copper oxide-based photobiocathode for Z-scheme semi-artificial leaf structure. *ChemSusChem* **13**, 2940–2944 (2020).
41. Kim, J. et al. Robust FeOOH/$BiVO_4$/Cu(In,Ga)Se_2 tandem structure for solar-powered biocatalytic CO_2 reduction. *J. Mater. Chem. A* **8**, 8496–8502 (2020).
42. Kim, J. et al. Unbiased photoelectrode interfaces for solar coupling of lignin oxidation with biocatalytic C=C bond hydrogenation. *ACS Appl. Mater. Interfaces* **14**, 11465–11473 (2022).
43. Grätzel, M. Photoelectrochemical cells. *Nature* **414**, 338–344 (2001).
44. Rudroff, F. et al. Opportunities and challenges for combining chemo- and biocatalysis. *Nat. Catal.* **1**, 12–22 (2018).

45. Lee, S. H., Choi, D. S., Kuk, S. K. & Park, C. B. Photobiocatalysis: activating redox enzymes by direct or indirect transfer of photoinduced electrons. *Angew. Chem. Int. Ed.* **57**, 7958–7985 (2018).
46. Le, T.-K. et al. Solar-powered whole-cell P450 catalytic platform for C-hydroxylation reactions. *ChemSusChem* **14**, 3054–3058 (2021).
47. Wang, D., Kim, J. & Park, C. B. Lignin-induced $CaCO_3$ vaterite structure for biocatalytic artificial photosynthesis. *ACS Appl. Mater. Interfaces* **13**, 58522–58531 (2021).
48. Son, G., Kim, J. & Park, C. B. Interference of solvatochromic twist in amyloid nanostructure for light-driven biocatalysis. *ACS Appl. Energy Mater.* **3**, 1215–1221 (2020).
49. Kim, J. et al. Biocatalytic C=C bond reduction through carbon nanodot-sensitized regeneration of NADH analogues. *Angew. Chem. Int. Ed.* **57**, 13825–13828 (2018).
50. Schmermund, L. et al. Photo-biocatalysis: biotransformations in the presence of light. *ACS Catal.* **9**, 4115–4144 (2019).
51. Hollmann, F., Arends, I. W. C. E. & Buehler, K. Biocatalytic redox reactions for organic synthesis: nonconventional regeneration methods. *ChemCatChem* **2**, 762–782 (2010).
52. Chen, H. et al. Fundamentals, applications, and future directions of bioelectrocatalysis. *Chem. Rev.* **120**, 12903–12993 (2020).
53. Ruff, A., Conzuelo, F. & Schuhmann, W. Bioelectrocatalysis as the basis for the design of enzyme-based biofuel cells and semi-artificial biophotoelectrodes. *Nat. Catal.* **3**, 214–224 (2020).
54. Ren, Y. et al. Strategies to suppress hydrogen evolution for highly selective electrocatalytic nitrogen reduction: challenges and perspectives. *Energy Environ. Sci.* **14**, 1176–1193 (2021).
55. Lin, C.-Y., Huang, S.-C., Lin, Y.-G., Hsu, L.-C. & Yi, C.-T. Electrosynthesized Ni–P nanospheres with high activity and selectivity towards photoelectrochemical plastics reforming. *Appl. Catal. B* **296**, 120351 (2021).
56. Perini, N. et al. Photoelectrochemical oxidation of glycerol on hematite: thermal effects, in situ FTIR and long-term HPLC product analysis. *J. Solid State Electrochem.* **25**, 1101–1110 (2021).
57. Mesa, C. A. et al. Kinetics of photoelectrochemical oxidation of methanol on hematite photoanodes. *J. Am. Chem. Soc.* **139**, 11537–11543 (2017).

Acknowledgements

This work was supported by the National Research Foundation (NRF) via the Creative Research Initiative Center (grant no. NRF-2015R1A3A2066191 (J.K., J.J. and C.B.P.)) and the Global PhD Fellowship Program (grant no. NRF-2019H1A2A1075810 (J.K.)), Republic of Korea.

Author contributions

J.K. conceived and designed the research, performed (photo)electrocatalytic/bioelectrocatalytic/photobiocatalytic experiments, analysed the data and wrote the manuscript. C.B.P. supervised the research. J.K., J.J. and C.B.P. discussed the photoelectrocatalysis. T.H. and F.H. provided J.K. and C.B.P. with the OYE and UPO enzymes. J.K., T.H. and F.H. commented on the biocatalysis. All authors contributed to revising the manuscript.

Competing interests

The authors declare no competing interests.

Additional information

Supplementary information The online version contains supplementary material available at https://doi.org/10.1038/s44160-022-00153-x.

Correspondence and requests for materials should be addressed to Chan Beum Park.

Peer review information *Nature Synthesis* thanks Hao Song and the other, anonymous, reviewer(s) for their contribution to the peer review of this work. Primary handling editor: Peter Seavill, in collaboration with the *Nature Synthesis* team.

Reprints and permissions information is available at www.nature.com/reprints.

Publisher's note Springer Nature remains neutral with regard to jurisdictional claims in published maps and institutional affiliations.

Springer Nature or its licensor holds exclusive rights to this article under a publishing agreement with the author(s) or other rightsholder(s); author self-archiving of the accepted manuscript version of this article is solely governed by the terms of such publishing agreement and applicable law.

© The Author(s), under exclusive licence to Springer Nature Limited 2022